Progress In Electromagnetics Research, Vol. 107, 269–292, 2010

SIGNAL RECOVERY IN PULSED TERAHERTZ INTEGRATED CIRCUITS

A. Heidari

T-Ray Science Inc.
405 King St., Waterloo, Ontario N2J 2Z4, Canada

M. Neshat, D. Saeedkia, and S. Safavi-Naeini

Electrical and Computer Engineering Department
University of Waterloo
Waterloo, Ontario N2L 3G1, Canada

Abstract—In this article, a time-domain calibration procedure is proposed for pulsed Terahertz Integrated Circuits (TIC) used in on-chip applications, where the conventional calibration methods are not applicable. The proposed post-detection method removes the unwanted linear distortions, such as interfering echoes and frequency dispersion, by using only one single-port measurement. The method employs a wave-transfer model for analysis of the TIC, and the model parameters are obtained by a proposed blind estimation algorithm. A complete implementation of the method is demonstrated for a fabricated TIC, when used in an on-chip sensing application. The features of interest in the measured signal, such as absorption lines, can be masked or weakened by the distortion of the THz signal happening in a TIC. The proposed signal recovery approach improves the detection of those otherwise hidden features, and can significantly enhance the performance of existing TICs. To show the effectiveness of the proposed de-embedding method, numerical results are presented for simulated and measured signals. The method presented in this article is enabling for accurate TIC applications, and can be utilized to optimally design novel TIC structures for specific purposes.

Received 18 March 2010, Accepted 18 May 2010, Scheduled 13 August 2010
Corresponding author: A. Heidari (aheidari@uwaterloo.ca).

1. INTRODUCTION

Terahertz (THz) technology [1, 2] is a fast-growing field with applications in biology and medicine [3], medical imaging [4], material spectroscopy and sensing [5], security, monitoring and spectroscopy in pharmaceutical industry, and high-data-rate communications. Situated between millimeter-wave and infrared range, the terahertz region with the frequency range from 100 GHz up to 10 THz is a scientifically rich but as yet not fully explored part of the electromagnetic spectrum.

Recent advances in THz circuit integration have opened up a wide range of possibilities in the on-chip applications [6–9]. However, several research challenges are yet to be overcome before development of the commercial products. One of the major challenges involves the algorithms used to efficiently extract the desired information from measured THz signals. The presented results in the literature show the need for more elaborate techniques for processing and analyzing of the THz signals, customized for each of the various applications.

Figure 1 shows a general structural diagram of a TIC chip. As conceptually shown in the diagram, the chip is constituted by interconnected circuit networks. It is assumed that a THz pulse is generated at one point on the chip and is detected at another point, after undergoing possible distortions due to interaction with the circuit networks. Other than the additive noises, THz pulses are distorted by passing through guiding structures and interacting with various components and materials in an integrated circuit. Different media alter THz waves based on their response characteristics. Assuming a linear interaction, the altered THz signal can be modelled as a *convolution* of the original THz signal and the impulse response of the medium. *Deconvolution*, which is a well-known problem in the processing of telecommunication signals, seismic signals, etc [10–

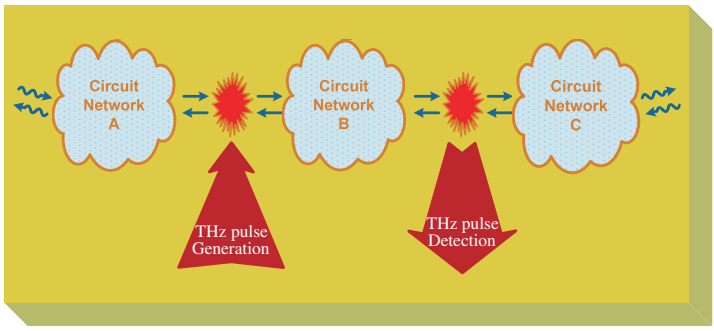

Figure 1. A general structural diagram of a TIC chip.

13], uses mathematical methods for estimation and removal of the convolutional effect of the medium or instrument from the altered signal. Echo Cancellation [14] is a popular branch of deconvolution methods.

Among the linear signal distortions in TICs, the most disabling effect is due to the presence of the echoed versions of the main signal in the measurements. In the sequel, the echo problem is explained, and then possible solutions and their limitations are discussed. In Section 2, we present a general method for modelling the distortions in TICs using two-port wave-transfer analysis. Then an estimation method for the model parameters is proposed, which only needs one single measurement of the output signal. The proposed calibration approach is demonstrated in details for a fabricated TIC, whose circuit layout is depicted in Fig. 6. The impact of the calibration on the performance enhancement of the TIC in a sensing application is also shown. The numerical results for simulated and measured signals are presented in Section 4.

1.1. The Echo Problem

The problem of having echoes arises when the original signal interferes with several echoes of itself reflecting from discontinuities. In optics, for example, a medium change in the path of the optical beam can cause a reflection. Same happens for an unmatched impedance in a transmission line. The echo problem is worse in TICs because the dimensions are short, and dispersion is typically severe. In general, depending on the optical setup or the TIC circuit layout, reflections can come from sample edges, wave-guide ends, source structure, detector structure, etc. In some cases, there may be more than one reflection mechanisms combined. Fig. 2 is a plot of a THz pulse measured in a TIC. After the main peak, two other major echoes are observable in the measurement period shown. The effect of frequency dispersion is also clearly visible on the echoes. These effects are modelled and quantified later on in this article.

Presence of unwanted echoes in a THz system can cause several problems. In frequency domain, the effect of echoes is similar to etalon effect, and a comb-like shape is imposed on the frequency components. This undesired effect is disabling for many applications, particularly for spectroscopy and sensing applications. Picosecond THz pulses contain a broadband frequency spectrum suitable for material spectroscopy and sensing. As the THz pulses interact with the sample under test, the rotational and vibrational resonance modes of molecular and crystalline structures of the material show up as absorption signatures in the spectrum, whereas in the temporal domain

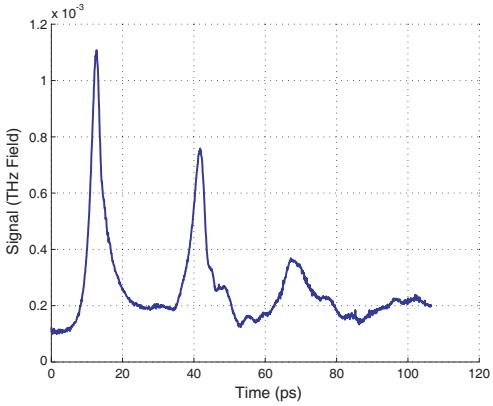

Figure 2. A sample of measured (pulse) signal in a TIC, including echoes coming from the discontinuities, frequency dispersion effect, and additive noise.

these signatures appear as small variations in the tail of the main pulse. Therefore, the spectroscopic information is contained in the temporal data collected after the main pulse. In such systems, the spectral resolution should be high enough to resolve all the existing absorption signatures. This can be achieved by increasing the time interval of the recorded signal. However, the maximum time interval is limited because of the interfering echoes arriving from the chip discontinuities. The interfering echoes affect all the frequency spectrum in a similar way as do the signatures, therefore, identification of signatures would be uncertain with the presence of interfering echoes.

1.2. Possible Solutions

Trivial solutions: One starting method is always trying to solve the problem in the hardware setup. Of course this is impossible in many cases, or at least costly if more expensive devices or new hardware designs are required. In fact there is a vast interest in software solutions lately as it is less costly and easier to implement. Terahertz Signal Processing is a new field to address such problems Terahertz systems.

A simple post-detection (signal processing) method for removing the echoes is to use a time-gating method. Evidently this will diminish the time-duration of the signal if the first echo closely follows the main peak. This method decreases the frequency resolution which is inversely proportional to the time-duration of the signal.

Using a reference signal: This method is currently the only viable solution to the problem. This approach utilizes extra

measurements to differentially remove the undesired effects, including echoes, from the signal [15]. To do this, the method requires a measurement from exactly the same setup, when the effect of interest is somehow removed [16]. In other words, one should make hardware modifications in order to remove the desired effect under measurement, and keep the unwanted effects. For example, in Ref. [15] the sample is substituted with a mirror to keep the echo structure the same.

However, this method is inconvenient and is not usually easy to implement. Modifying the hardware setup is time-consuming and costly. In many cases it is not even possible. For example, when the sample structure itself causes the echoes. Another example is a TIC where changing the structure is not possible. Furthermore, this approach may have undesirable effects for some applications as it eliminates every feature of the measured signal that is present in the reference.

Blind Echo Cancelation: Here is a more general solution to the echo problem. The overall multi-reflection mechanism can be modelled as an input-output system, as depicted in Fig. 3. In this model, the input $x_g(t)$ is the signal without any interfering echoes, and the output is the measured signal $x_m(t)$ which has gone through multiple reflections. In a TIC, the output signal is directly measurable whereas the input signal is not accessible to be measured and is not a priori known, but is to be estimated. It is assumed that the echo system is a linear time-invariant system.

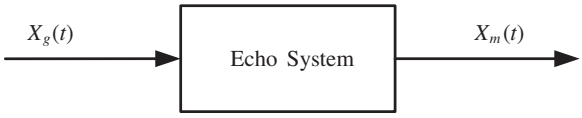

Figure 3. A systematic diagram of an echo system.

Assuming there is *no frequency dispersion*, impulse response of the echo system can be given as

$$h_m(t) = \sum_{p=0} \alpha_p \, \delta\left(t - \tau_p\right), \tag{1}$$

where α_p and τ_p represent the relative amplitude and delay time of the p'th reflection, respectively. Equivalently, the output signal is derived as

$$x_m(t) = h_m(t) \star x_g(t) \tag{2}$$

$$= \sum_{p=0} \alpha_p \, x_g\left(t - \tau_p\right) \tag{3}$$

where $\star$ is the convolution operator. For this non-dispersive case, α_p and τ_p for each echo can be directly estimated from the measured signal $x_m(t)$, then $x_g(t)$ is recovered by applying a *deconvolution* algorithm in time or frequency domain [17].

In a *dispersive medium*, the propagation and reflection mechanisms are frequency dependent. Therefore, various frequency components are reflected from the discontinuities differently, and travel at different velocities. In this case, the impulse response of the echo system can not be estimated solely from the measured signal without any knowledge on the behavior of the dispersive mechanisms involved. In the sequel, we propose an approach to solve such problems by analyzing the dispersive characteristics of the echo mechanism, and any other type of linear distortion. The proposed method is demonstrated by introducing a model for the overall transfer function between any input-output points in a TIC where the unaccessible input signal is desired to be estimated from the measurable output signal. Then, the parameters of the model are estimated from the measured output signal using a proposed optimization criterion.

It is notable that in the literature, the presence of the echoes (etalon effect) has been utilized for some applications, for example, for characterization of unknown samples in a THz TDS system. Interested reader may refer to [18, 19] and the references therein.

2. MODELLING THE SIGNAL DISTORTIONS IN A TIC

Figure 1 shows a general demonstration of a TIC as explained before. A majority of the TIC's can be depicted in more details as shown in Fig. 4, assuming a two-port model for every circuit element, and a one-port input and output. A signal is generated and coupled to the circuit. The froward and backward traveling waves become distorted by going through the circuit networks (typically experiencing successive propagations and reflections ...), and eventually the summation is detected as the measurable output signal. Usually a calibration procedure is applied to remove such unwanted distortions. However, the conventional calibration methods need access to both ports in the two-port input and output which is not possible here. Moreover, the calibration is performed in frequency domain for continuous wave (not pulsed wave) exciting signals as, for example, in vector network analyzers.

In this article, we propose a post-detection method to remove the aforementioned distortions from the signal. A *single* measurement is used to identify the effect of a two-port system on the signal. The proposed method can be considered as a time-domain calibration

procedure.

2.1. The Wave-transfer Model

Figure 4 depicts a wave-transfer diagram [20] for a single pulse in a TIC. The input X_g is the THz wave (in frequency domain) that is generated and coupled to the forward and backward directions. Assuming a coupling factor κ, we have $X_{if} = \kappa\, X_g$, representing the input signal coupled in the forward direction, and $X_{ib} = (1-\kappa)X_g$ coupled in the backward direction. On the other hand, X_{of} and X_{ob}, the forward and the backward constituents of the output, are added and detected as the measured signal $X_m = X_{of} + X_{ob}$. For *Reflecting Component I* and *Reflecting Component II* blocks, the unconnected input represents the noise and interference, and the unconnected output represents the radiated signal.

For the *Propagation* L_i block, $i = 0, 1, \ldots, 5$, the wave-transfer matrix is $\begin{bmatrix} P_i(\omega) & 0 \\ 0 & P_i^{-1}(\omega) \end{bmatrix}$, where

$$P_i(\omega) \triangleq \exp\left(-\xi(\omega)\, L_i\right), \tag{4}$$

and $\xi(\omega) = \alpha(\omega) + j\,\beta(\omega)$ represents the attenuation (real part) and the phase constant (imaginary part) of the transmission line, and L_i is the propagation length in each segment.

2.2. Derivation of the Transfer Function

For our measurement system, the model shown in Fig. 4 can be simplified. We assume that the sensor behaves as a number of band-reject filters at the absorption lines, therefore, the wave-transfer matrix can be shown as $\begin{bmatrix} I(\omega) & 0 \\ 0 & I^{-1}(\omega) \end{bmatrix}$, where $I(\omega)$ is the frequency

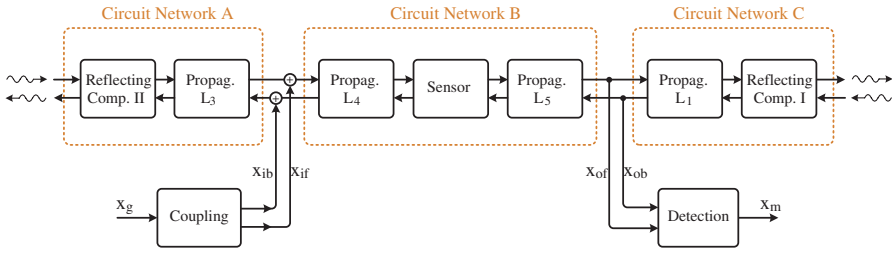

Figure 4. A complete wave-transfer diagram of a typical TIC with a sensor.

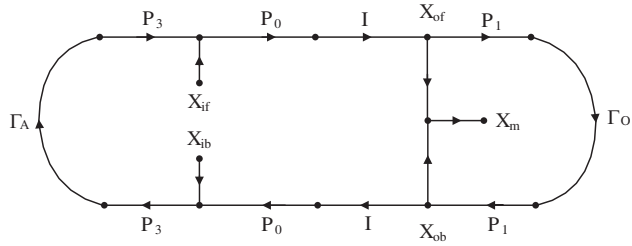

Figure 5. The equivalent frequency-domain signal flow graph of the TIC shown in Fig. 4.

response of the sensor including the absorption lines of the sample. Also $L_0 \triangleq L_4 + L_5$, and $L_2 \triangleq L_0 + L_3$. For *Reflecting Component I* and *-II*, the input noise and interference is ignored. With these assumptions, the model can be simplified as shown in Fig. 5. $\Gamma_O(\omega)$ and $\Gamma_A(\omega)$ are the reflection coefficients of *Reflecting Component I* and *-II*, respectively.

Consider the two-input two-output system in Fig. 5. Then,

$$\begin{bmatrix} X_{of}(\omega) \\ X_{ob}(\omega) \end{bmatrix} = \mathbf{M}(\omega) \begin{bmatrix} X_{if}(\omega) \\ X_{ib}(\omega) \end{bmatrix} \tag{5}$$

where

$$\begin{aligned} \mathbf{M}(\omega) &= \begin{bmatrix} m_{ff}(\omega) & m_{fb}(\omega) \\ m_{bf}(\omega) & m_{bb}(\omega) \end{bmatrix} \\ &= \frac{H_0(\omega)\, I(\omega)}{1 - H_1(\omega)\, H_2(\omega)\, I^2(\omega)} \begin{bmatrix} 1 & H_3(\omega) \\ H_1(\omega) & H_1(\omega)\, H_3(\omega) \end{bmatrix} \end{aligned} \tag{6}$$

The above formula is derived by using the signal flow analysis from each of the two inputs to each of the two outputs. To observe the effects of the different parts of the circuit, the important subsystems of the TIC signal flow diagram are defined as follows,

- $H_0(\omega) = P_0(\omega)$: denoting the (propagation) transfer function from the generation site to the detection site (G $\mapsto$ D);
- $H_1(\omega) = {P_1}^2(\omega)\, \Gamma_O(\omega)$: denoting the transfer function from the detection site to the detection site through *Reflecting Component I* of the transmission line (D $\mapsto$ *Reflecting Component I* $\mapsto$ D);
- $H_2(\omega) = {P_2}^2(\omega)\, \Gamma_A(\omega)$: denoting the transfer function from the detection site to the detection site through *Reflecting Component II* (D $\mapsto$ *Reflecting Component II* $\mapsto$ D);

- $H_3(\omega) = {P_3}^2(\omega)\,\Gamma_A(\omega)$: denoting the transfer function from the generation site to the generation site through *Reflecting Component II* (G $\mapsto$ *Reflecting Component II* $\mapsto$ G).

The overall transfer function, as depicted in Fig. 3, is defined as

$$H(\omega) = \frac{X_m(\omega)}{X_g(\omega)}. \tag{7}$$

Hence, from (5) we can write

$$H(\omega) = \begin{bmatrix} 1 & 1 \end{bmatrix} \mathbf{M}(\omega) \begin{bmatrix} \kappa \\ 1-\kappa \end{bmatrix} \tag{8}$$

$$= \frac{H_0(\omega)\,\{1 + H_1(\omega)\}\,I(\omega)}{1 - H_1(\omega)\,H_2(\omega)\,I^2(\omega)}\,\{\kappa + (1-\kappa)\,H_3(\omega)\} \tag{9}$$

It is notable that the transfer function $H(\omega)$ actually models the overall signal distortion of the circuitry, including the multi-reflection phenomenon and dispersion, in the frequency domain. In (9), $\kappa = 1$ minimizes the distortion. For simplicity, this assumption is considered in the sequel, and so the value of $H_3(\omega)$ becomes irrelevant. Also the Generation site could be moved such that $L_3 = 0$. Nevertheless, the proposed analysis is applicable to the general case.

To calculate the transfer function $H(\omega)$, the following physical parameters are needed for the frequency range of interest: $\xi(\omega)$, $\Gamma_O(\omega)$ and $\Gamma_A(\omega)$. These parameters could be obtained by analytical methods or by numerical simulation of the TIC structure. Furthermore, the values of the distance parameters L_0, L_1 and L_2 are needed.

3. BLIND ESTIMATION OF THE MODEL PARAMETERS

To identify the transfer function $H(\omega)$, the values of propagation lengths L_0, L_1 and L_2 are needed. These values are specified by the points where the pump and probe laser beams are shined on the chip at the generation and detection sites, in a conventional photoconductive generation-detection approach. The nominal values of these parameters are normally available from the measurement setting. However, the effective values of these parameters specifying the transfer function may be different. One reason is that in practice the generation and detection sites can not be located with high precision. Another reason is that the effective length of the transmission lines might be different from their physical lengthes because of the end effects. Also the estimate of the effective refractive index is not exact. Other environmental factors might affect these

values too. As a result, these parameters need to be estimated from the output signal itself. Note that there is no reference signal available here, therefore we need to accommodate a blind estimation method for the parameters.

By looking at the relations of these parameters to the transfer function $H(\omega)$, it is observed that L_1 and L_2 have more significant impacts compared to L_0. In fact, variations in L_0 mainly result in some time shift in the output signal, and do not affect the periodicity of the echoes. This means that a meaningful estimation of L_0 from the output signal is not also possible as the signal does not carry much information about L_0. For this reason, we will estimate L_1 and L_2 from the output signal, and use the nominal value for L_0.

Assuming $\hat{L}_1$ and $\hat{L}_2$ are estimated values of the corresponding model parameters, we propose the following cost function

$$J(\hat{L}_1, \hat{L}_2) = \| \hat{x}_g(t) \|_{l2}^2, \quad T_0 < t < T_1, \tag{10}$$

where $\| \cdot \|_{l2}$ is the l_2-norm. This cost function represents the energy of the residual echoes remaining in the estimated signal $\hat{x}_g(t)$. The threshold T_0 is roughly set to a time point after the high-energy part of the pulse, to only include the effect of the remaining echoes after the deconvolution process, and T_1 is normally limited to the time duration of the measured signal. Two samples of the cost function are plotted in Fig. 10 and Fig. 12 as explained later in the numerical results. The proposed cost function is blind, meaning that it does not need any reference signal to calculate the error. Having the cost function, an optimization method is adopted to find $\hat{L}_1$ and $\hat{L}_2$ values that minimize $J(\hat{L}_1, \hat{L}_2)$. It is shown in Appendix A that the function $J(\hat{L}_1, \hat{L}_2)$ is locally convex around the optimum point. For a typical pulse, the cost function is also globally minimized at the optimal point. Therefore, to find the optimal point in $L_1 - L_2$ space, a grid search of the minimum point is sufficient, and is practically feasible as well because the computational complexity of the cost function is low. For higher accuracies, the values can be fine-tuned near the optimal point using convex optimization methods.

3.1. Extraction of the Sensing Information

As explained in the previous section, the model parameters are estimated from the measured signal x_m in the time domain. It is shown in Section 4.3 that the proposed parameter estimation method is robust to additive noise and small perturbations. This means that presence of a sensor $I(\omega)$, for example, with a few typical absorption lines, has no effect on the performance. Therefore, the transfer function

can be identified as if the sensor is not present. The formulation is then followed from (9) where $I(\omega)$ is substituted with 1, i.e.,

$$\hat{H}(\omega) = \frac{H_0(\omega)\ \{1 + H_1(\omega)\}}{1 - H_1(\omega)\, H_2(\omega)} \tag{11}$$

Therefore, $X_g(\omega)$ is estimated by deconvolution as

$$\hat{X}_g(\omega) = \frac{X_m(\omega)}{\hat{H}(\omega)} \tag{12}$$

$$= U(\omega) X_g(\omega) \tag{13}$$

where $U(\omega) \triangleq \frac{H(\omega)}{\hat{H}(\omega)}$.

The absorption lines are typically present at a few discrete frequency regions, where

$$U(\omega) = I(\omega)\, \frac{1 - H_1(\omega)\, H_2(\omega)}{1 - H_1(\omega)\, H_2(\omega)\, I^2(\omega)}, \tag{14}$$

whereas at other frequencies $U(\omega) = 1$. At an absorption frequency, $I(\omega) \ll 1$. Also normally $|H_1(\omega)\, H_2(\omega)| < 1$. Hence, the denominator in (14) is negligible there, and so $U(\omega)$ is proportional to $I(\omega)$. This means that the effect of the absorption lines are directly observable on $\hat{X}_g(\omega)$, while other unwanted distortions are removed. From a systematic point of view, as if $x_g(t)$ has gone through the sensor and is detected as $\hat{x}_g(t)$, in an environment free of echo and other distortions.

When a TIC is employed for a sensing or spectroscopy application, the undesired distortions mask or weaken the desired perturbation-like features such as absorption lines. The proposed method can be used to enhance the sensitivity in such applications by removing or decreasing the effect of undesired distortions, and optimally estimate $I(\omega)$ from the provided formulations. In detection of the absorption lines, for example, it may be possible to achieve further resolution by an accurate estimation of $I(\omega)$ from (14). If $X_g(\omega)$ is assumed to be smooth (which is a practically reasonable assumption), $X_g(\omega)$ can be approximated by a locally-smoothed version of $\hat{X}_g(\omega)$, and $U(\omega)$ is estimated. Because $H_1(\omega)$ and $H_2(\omega)$ are already identified, we can tap into (14) and find $I(\omega)$ by solving a second degree polynomial at each ω. We will show the results for both methods in the following section.

4. NUMERICAL RESULTS

In this section, the performance of the proposed method is evaluated, by using simulated and measured signals. In the following, a fabricated

multi-purpose TIC is described. The structural diagram of the TIC is the same as shown in Fig. 4 where *Reflecting Component I* is an "open end", and *Reflecting Component II* is an "antenna". Then the TIC is used as an example to show how the recovery method, proposed in this article, works when the TIC is utilized in an on-chip sensing application.

4.1. The Structure of Our TIC

In a pulsed TIC, transmission lines and other planar components are formed by the metallic patterns on a multilayer substrate for guiding and controlling (sub)picosecond THz pulses. Fig. 6 shows the metal pattern of a fabricated THz chip containing a coplanar stripline (CPS) transmission line with open end on one side and terminated to a bow-tie antenna on the other side. The CPS is 2.7 mm long with the metal traces of 20 μm width, separated by 10 μm. The fast photoconductive material is a 100 nm-thick low-temperature grown GaAs (LTG-GaAs) grown on a 150 μm-thick S.I. GaAs substrate. THz pulse generation-detection in this chip is based on the interaction of femtosecond laser pump-probe beams with the fast photoconductor layer. A standard pump-probe measurement setup was used for on-chip THz pulse generation and detection, as shown in Fig. 7. The laser source is a 780 nm Ti:sapphire femtosecond laser with pulse duration of 100 fs, and 80 MHz repetition rate. It illuminates the generation site on the chip for pulse generation. A part of the energy of the generated THz pulse is coupled into the CPS, and propagates toward

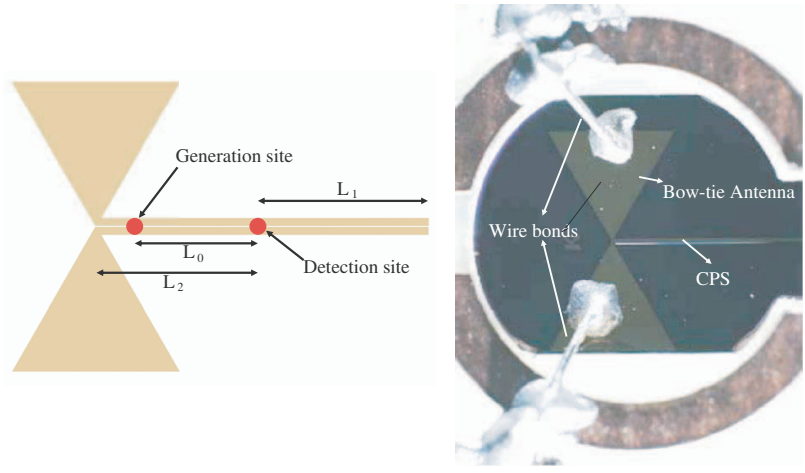

Figure 6. Circuit layout and photo of the fabricated TIC chip.

the detection site. In this analysis, the antenna is treated as a loading impedance for the CPS. The probe beam passes through a variable delay line, and is focused on the center of the CPS (detection site) for pulse detection. In Fig. 2, the detected THz pulse including the main pulse and two echoes is shown. The first echo shown in Fig. 2 is the result of the reflection of the main pulse from the open end, and the second echo is due to the reflection of the first echo from the antenna side.

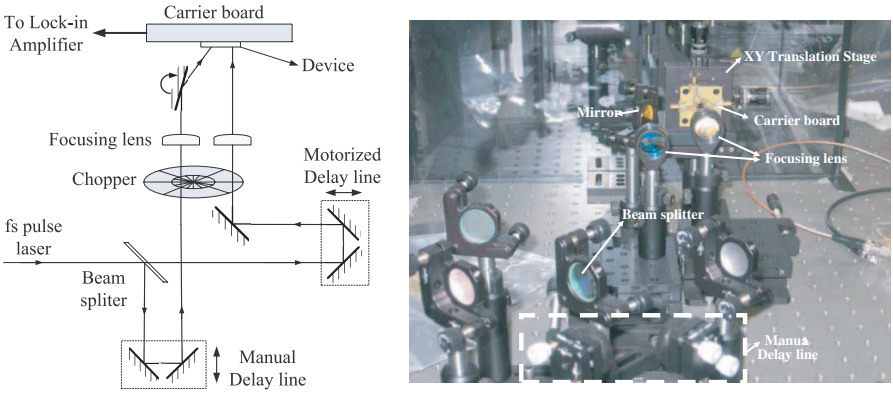

Figure 7. The schematics and photo of the THz setup to test the TIC.

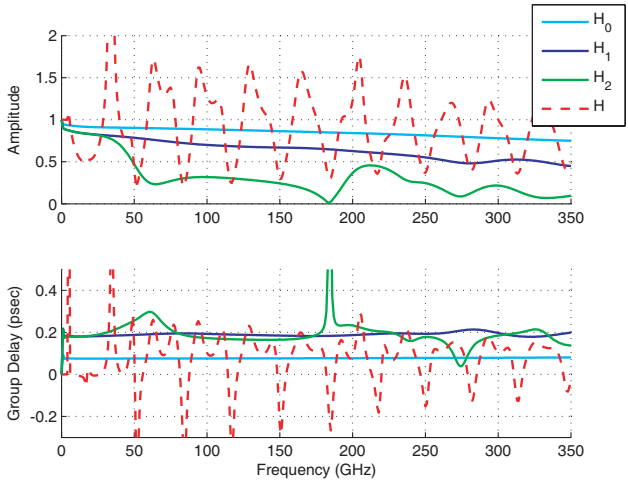

Figure 8. The amplitude and the group delay of the frequency response for the subsystems and the total transfer function of our TIC.

To quantify the dispersion parameters and the reflection coefficients at different frequencies, we have numerically simulated our TIC structure shown in Fig. 6. The parameters $\alpha(\omega)$, $\beta(\omega)$, $\Gamma_A(\omega)$ and $\Gamma_O(\omega)$ are calculated using the ADS Momentum, a commercial electromagnetic simulator based on Method of Moment [21], for the frequencies up to 350 GHz.

The nominal physical parameters of our TIC are as follows: $L_0 = L_1 = L_2 = 1.35$ mm, and the effective refractive index is computed as 2.51. To achieve $\kappa = 1$ in practice, the Generation site is moved to the CPS-Antenna joint, i.e., $L_3 = 0$ as assumed in the analysis before. Fig. 8 shows the amplitudes and the group delays of the important subsystems, and $H(\omega)$ calculated from the aforementioned physical parameters. In this plot it is assumed that $I(\omega) = 1$, and the nominal values of the parameters are used.

4.2. Results

To evaluate the proposed recovery algorithm, we employ two simulated examples where the algorithm is applied on the output signals $x_m(t)$ of a simulated TIC. Each simulated output signal is numerically calculated from the convolution of a given input signal $x_g(t)$ and the impulse response of the echo system $h(t)$ in the TIC. This way, the estimated signal obtained by applying the recovery algorithm can be directly compared with the initially given input signal. In these simulated examples, the given input signals are selected from separate THz measurements. The nominal specifications of our TIC are used for these simulations, and the frequency response $H(\omega)$ is calculated as shown in Section 2.2. Also $I(\omega)$ is defined to include three band-reject filters, resembling existence of three different absorption lines in the sensor of the simulated TIC, as follows: a 3 GHz, -10 dB absorption at 190 GHz, a 3 GHz, -5 dB absorption at 287 GHz, and a 1 GHz, -2 dB absorption at 150 GHz. Then, the impulse response in time-domain $h(t)$ is calculated, which is used in both simulated cases I and II, discussed in what follows.

For each simulation, a given input pulse $x_g(t)$ is convolved with the calculated $h(t)$ to generate the simulated output signal $x_m(t)$. This operation imposes the linear distortions of the TIC on the input pulsed signal, i.e., the resulting $x_m(t)$ is a superposition of several delayed and dispersed echoes as seen in the following results. Fig. 9 shows the results for signal I, in time-domain and in frequency-domain. In this case, $x_g(t)$ is a wide-band THz pulse measured in a separate free-space THz time-domain setup. $x_m(t) = h(t) \star x_g(t)$ as explained, and $\hat{x}_g(t)$ is achieved using the proposed recovery method on $x_m(t)$. The respective two-dimensional cost function $J(L_1, L_2)$ is plotted in Fig. 10. The

$L_1 - L_2$ space is searched on the 1%-precision grids to find the minimum point of the cost function (indicated with a red cross). Then the found values are used to calculate the frequency response $\hat{H}(\omega)$, and then to recover $\hat{x}_g(t)$ signal using frequency domain deconvolution. Needless to say that as the blind nature of the proposed method implies, only $x_m(t)$ is used in the recovery process. To evaluate the recovery performance for the simulated cases, the normalized error power is calculated over the frequency range of interest, as follows,

$$\text{NMSE} = \frac{\int_{\omega_1}^{\omega_2} \left| \hat{X}_g(\omega) - X_g(\omega) \right|^2 d\omega}{\int_{\omega_1}^{\omega_2} \left| X_g(\omega) \right|^2 d\omega}. \tag{15}$$

Here, $\omega_1 = 100\,\text{GHz}$ and $\omega_2 = 350\,\text{GHz}$. It is notable that to decrease the effect of the noise and spurious components, the signal bands bellow 10 GHz and above 350 GHz are filtered out before the recovery process.

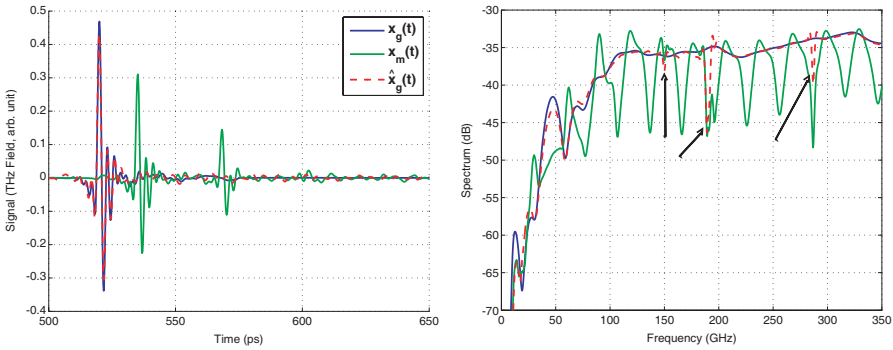

(a) (b)

Figure 9. The result for signal I, (a) in time domain, and (b) in frequency domain. The three absorption lines are indicated by arrows.

Similarly, Fig. 11 shows the results for signal II. The $x_g(t)$ used in this case is a THz pulse constructed by time-gating the main peak in the measured signal shown in Fig. 2, and then applying a low-pass filter to remove the artifacts. The reason for using this method to manually produce such signal is that we wanted to provide simulation results similar to the measurement from our TIC. The respective cost function is plotted in Fig. 12 as well. It is observed that in both simulations, the parameters are correctly estimated and $\hat{x}_g(t)$ is accurately recovered. Also all three absorption lines are clearly visible on the recovered signal in the frequency domain, whereas they are buried or partially masked

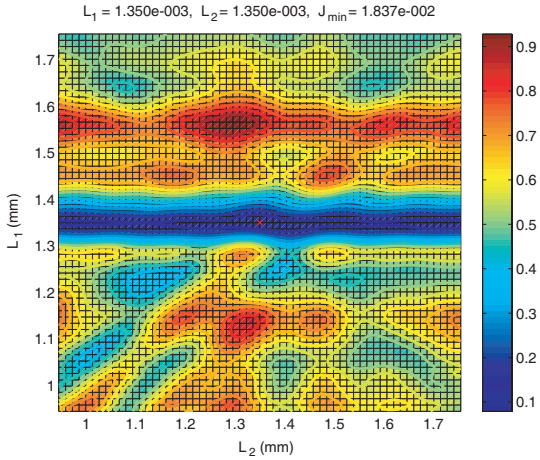

Figure 10. The cost function $J(L_1, L_2)$ for signal I.

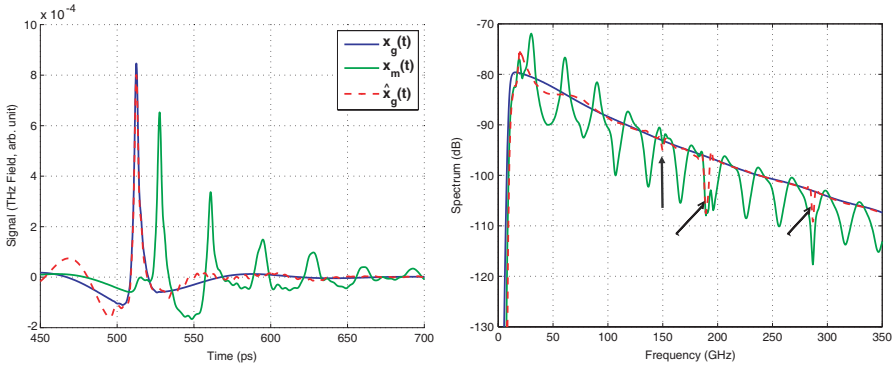

Figure 11. The result for signal II, (a) in time domain, and (b) in frequency domain. The three absorption lines are indicated by arrows.

in $X_m(\omega)$. Later it is shown how this information can be efficiently extracted from the result.

Figure 13 shows the detected absorption lines for signal II, using the method discussed in Section 3.1. The results are achieved by approximating $X_g(\omega)$ by running a zero-delay moving-average filter on $\hat{X}_g(\omega)$. Next, $U(\omega) = \frac{\hat{X}_g(\omega)}{X_g(\omega)}$ is estimated, which is plugged in (14) to find $I(\omega)$ by solving the second-degree polynomial equation for each ω over the frequency range of interest. For our TIC, $|H_1(\omega)H_2(\omega)| \ll 1$ over the frequency range of 100–350 GHz. Therefore, $U(\omega) \cong I(\omega)$

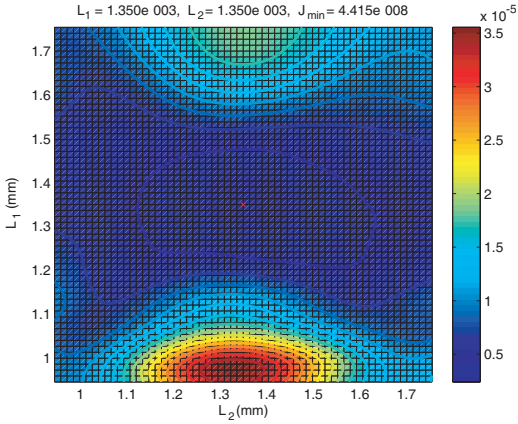

Figure 12. The cost function $J(L_1, L_2)$ for signal II.

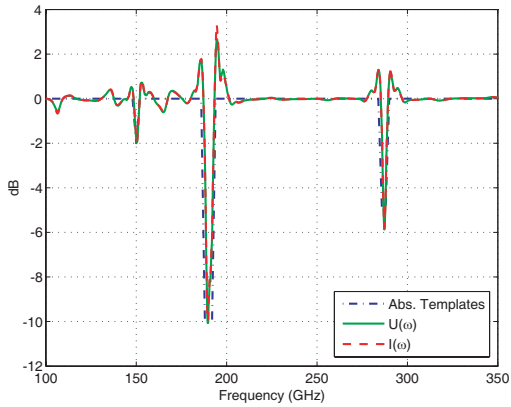

Figure 13. Accurate detection of the absorption lines.

as predicted by (14), and the latter calculation gives very similar results as the approximation. However, in general, $U(\omega)$ is a biased approximation of the absorption, and the discrepancy between $U(\omega)$ and $I(\omega)$ is significant if $|H_1(\omega)H_2(\omega)|$ is close to 1. In any case, $I(\omega)$ is the optimal estimate which can be calculated as proposed here.

As seen above, the recovery algorithm is successfully tested in the simulated cases. For a complete evaluation of the modelling part, as well as the recovery algorithm, we performed a measurement using an early version of our TIC. No sensors were present for these measurements. Fig. 14 shows the result of applying our method to the measured signal, in both time-domain and frequency-domain. Fig. 15 depicts the respective cost function.

As discussed before, the recovered signal $x_g(t)$ may potentially have a time delay with respect to $\hat{x}_g(t)$, because of the blind nature of the method which is not sensitive to the delay caused by L_0. In the simulated cases, it is observed that there is no time-delay error as L_0 is exactly known, however this delay can not be determined for a real measurement where $x_g(t)$ is not available. However, this delay is constant for a specific TIC and can be exactly determined. For the measured signal, as observed in the time domain plot of Fig. 14, the recovery algorithm has rather well removed the first echo which has the strongest disturbing effect. Looking at the result in the frequency domain, the comb-like fluctuations of $X_m(\omega)$ have a deviation of about 15 dB, while the recovered signal $\hat{X}_g(\omega)$ have a deviation of around 5 dB. In a sensing application, for example, this improves the detection capability of weak signatures which may have been masked, and also enhances the accuracy of the sensing method. Nevertheless, the non-ideal performance of the recovery method is mainly due to modelling errors (i.e., the difference between the actual mechanism and the applied model), and also possibly from measurement noises and interferences.

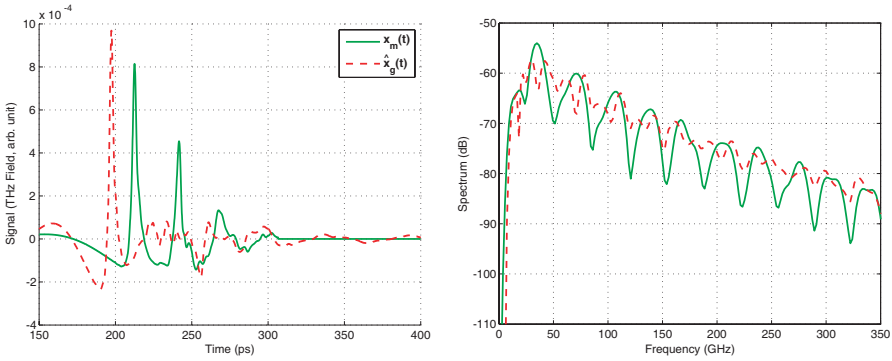

Figure 14. The result for the measured signal, (a) in time domain, and (b) in frequency domain.

As for the frequency dispersion effect, all the echoes experience widening to some degree, more for the latter echoes which travel longer distances in the dispersive medium. By comparing the recovered pulse $\hat{x}_g(t)$ with the main peak (echo number 0) of $x_m(t)$, we observe a 5% decrease in the pulse-width because of the recovery process. The reason for this, is that the proposed method is compensating for the dispersion effect as well.

Table 1 is a brief comparison of the results, summarizing NMSE

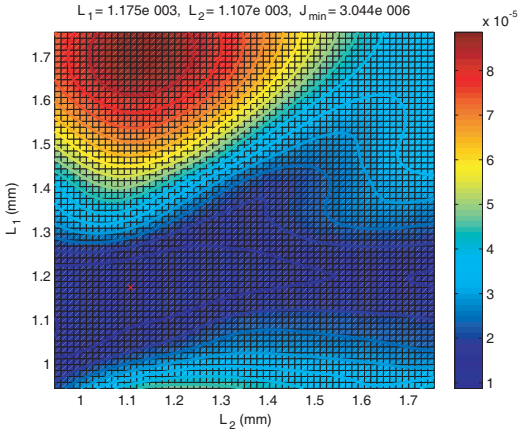

Figure 15. The cost function $J(L_1, L_2)$ for the measured signal.

Table 1. Comparison of NMSE and $J_{\min}$.

		NMSE	$J_{\min}$
Signal I:	without abs.	0.15%	2.16e-3
	with abs.	2.1%	1.82e-2
Signal II:	without abs.	0.19%	3.36e-8
	with abs.	1.7%	4.42e-8
Measured Signal		unknown	3.04e-6

and $J_{\min}$. For each simulated signal, when the absorption lines are added, the normalized recovery error NMSE contains the power of the absorption lines (which are present in $\hat{X}_g(\omega)$ but not in $X_g(\omega)$), and so NMSE is higher in this case. A similar effect is imposed on the cost function as seen from $J_{\min}$ values, because absorption lines add some ripples to the signal in time-domain (observable in Figs. 9 and 11) which is reflected in the values of cost function. Sensitivity of the proposed cost function to such perturbations is quantified in the next section. For the measured signal, it is ideally expected to see a $J_{\min}$ similar to the simulated signal II. The difference observed in the table comes from modelling errors and measurement noises.

4.3. Sensitivity to Noise

To examine the sensitivity of the algorithm to noise and perturbations, we added white Gaussian noise (AWGN) to the simulated signals $x_m(t)$

before the recovery process. By testing in several simulation runs, the parameter values L_1 and L_2 are correctly estimated within 1% error, as long as signal-to-noise power ratio (SNR) is larger than a threshold, namely, for signal I, SNR ≥ 7 dB, and for signal II, SNR ≥ 5 dB. This means that weak or moderate noise and perturbations do not have any effect on the estimation of parameter values which is the key part of the proposed method.

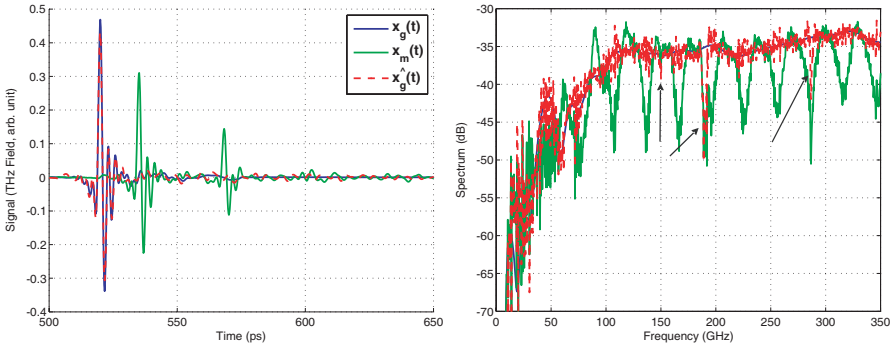

(a) (b)

Figure 16. The result for signal I when white Gaussian noise is added with SNR = 15 dB, (a) in time domain, and (b) in frequency domain. The three absorption lines are indicated by arrows.

Figure 16 shows the recovery results for signal I when white Gaussian noise is added with SNR = 15 dB. Despite the visibility of the noise in the frequency domain, two of the absorption signatures are easily distinguishable. Although the recovery process is robust to additive noise as stated above, weak signatures in the recovered signal may be obscured by noise residues.

4.4. Conclusion

In this article, a method is proposed to remove the unwanted linear distortions of a TIC from a single measured signal. In fact, the post-detection signal processing method is a time-domain calibration procedure for TICs where conventional calibration is impossible. An implementation of the method is shown for a sensing application of a fabricated TIC.

The contributions and benefits of the method proposed in this article can be summarized as follows:

- A time-domain calibration procedure is introduced.

- It is a post-detection signal processing method, which can be implemented in software or hardware.
- A TIC is identified using one single-port measurement.
- To estimate the model parameters, a blind time-domain method is proposed.
- The presented analysis can be utilized to virtually measure the internal nodes of a TIC.
- It is shown that, for example, in a sensing or spectroscopy application, the performance can be enhanced by using the proposed method.
- The proposed approach in this article can be used as a design guideline as well. To design a TIC intended for a specific application, the proposed analysis can provide the optimal way for the design of the different components of the TIC, and for the efficient utilization of it for the application.

ACKNOWLEDGMENT

This work is supported by T-Ray Science Inc., Natural Sciences and Engineering Research Council of Canada (NSERC), Research in Motion (RIM), CMC Microsystems, and Ontario Centers of Excellence (OCE).

APPENDIX A. ON CONVEXITY OF THE COST FUNCTION

In the noise- and perturbation-free case, the deconvolved reference signal can be written as

$$\hat{X}_g(\omega) = U(\omega)\, X_g(\omega), \tag{A1}$$

where

$$U(\omega) = \frac{H(L_1, L_2, \omega)}{H(\hat{L}_1, \hat{L}_2, \omega)}, \tag{A2}$$

is the overall effect of the echo system and the inverse system estimated by our method. Ideally, $U(\omega) = 1$, however $U(\omega)$ depends on the accuracy of parameter estimation, as shown in the sequel.

Assuming a small perturbation around the optimal point, we write $\hat{L}_1 = L_1 + \Delta L_1$ and $\hat{L}_2 = L_2 + \Delta L_2$, where $\Delta L_1 \ll L_1$ and $\Delta L_2 \ll L_2$. Therefore, $H(\hat{L}_1, \hat{L}_2, \omega) \cong H(L_1, L_2, \omega) + \Delta L_1 \frac{\partial}{\partial L_1} H(L_1, L_2, \omega) + \Delta L_2 \frac{\partial}{\partial L_2} H(L_1, L_2, \omega)$. Hence we can write

$$U(\omega) \cong 1 - \Delta L_1\, Q_1(\omega) - \Delta L_2\, Q_2(\omega), \tag{A3}$$

where

$$Q_i(\omega) \triangleq \frac{\frac{\partial}{\partial L_i} H(L_1, L_2, \omega)}{H(L_1, L_2, \omega)}, \quad i = 1, 2. \tag{A4}$$

Respectively, in the time domain we have

$$u(t) \cong \delta(t) - \Delta L_1\, q_1(t) - \Delta L_2\, q_2(t). \tag{A5}$$

Therefore,

$$\hat{x}_g(t) = u(t) \star x_g(t) \tag{A6}$$

$$\cong x_g(t) - \Delta L_1\, r_1(t) - \Delta L_2\, r_2(t), \tag{A7}$$

where $r_i(t) \triangleq q_i(t) \star x_g(t)$ for $i = 1, 2$.

Now the proposed cost function can be written as

$$J(\hat{L}_1, \hat{L}_2) = \int_{T0}^{T_1} |\hat{x}_g(t)|^2\, dt \tag{A8}$$

$$\begin{aligned} \cong & \int_{T0}^{T_1} |x_g(t)|^2\, dt \\ & + (\Delta L_1)^2 \int_{T0}^{T_1} |r_1(t)|^2\, dt + (\Delta L_2)^2 \int_{T0}^{T_1} |r_2(t)|^2\, dt \\ & - 2\Delta L_1 \int_{T0}^{T_1} x_g(t)\, r_1(t) dt \\ & - 2\Delta L_2 \int_{T0}^{T_1} x_g(t)\, r_2(t) dt \end{aligned} \tag{A9}$$

Note that all the approximations in this appendix become exact when $\Delta L_1, \Delta L_2 \to 0$.

Assume that $x_g(t)$ is a typically good pulse. This means after the main peak (i.e., for $t > T_0$), $x_g(t)$ has small values oscillating around zero. Therefore, the cross-terms in (A9) are ignorable. Hence,

$$J(\hat{L}_1, \hat{L}_2) \cong J_{\min} + R_1\, (\Delta L_1)^2 + R_2\, (\Delta L_2)^2 \tag{A10}$$

where $J_{\min} = \int_{T0}^{T_1} |x_g(t)|^2\, dt$ is the minimum of the cost function which happens at $\Delta L_1 = \Delta L_2 = 0$, and $R_i = \int_{T0}^{T_1} |r_i(t)|^2\, dt$, $i = 1, 2$, are positive constants. It is observed from (A10) that the cost function is a quadratic convex function around the optimal point.

Here we showed that the optimal point is a *local minima* of the proposed cost function, however, we generally can not say anything about it being the *global minima*. This is of interest in cases where the nominal values of L_1 and L_2 are not known. If $x_g(t)$ is a fairly good pulse which dominant energy is confined in time, and T_0 is properly

selected to a time after the dominant part of $x_g(t)$, it is observed that the global minima of the cost function is the optimal point, and so the algorithm becomes robust to the modelling errors appearing in the nominal values of L_1 and L_2.

REFERENCES

1. Tonouchi, M., "Cutting-edge terahertz technology," *Nature Photonics*, Vol. 1, No. 2, 97–105, 2007.
2. Siegel, P., "Terahertz technology," *IEEE Transactions on Microwave Theory and Techniques*, Vol. 50, No. 3, 910–928, 2002.
3. Siegel, P., "Terahertz technology in biology and medicine," *IEEE Transactions on Microwave Theory and Techniques*, Vol. 52, No. 10, 2438–2447, 2004.
4. Mittleman, D., M. Gupta, R. Neelamani, R. Baraniuk, J. Rudd, and M. Koch, "Recent advances in terahertz imaging," *Applied Physics B: Lasers and Optics*, Vol. 68, No. 6, 1085–1094, 1999.
5. Beard, M., G. Turner, and C. Schmuttenmaer, "Terahertz spectroscopy," *Journal of Physical Chemistry B*, Vol. 106, No. 29, 7146–7159, 2002.
6. Wood, C., J. Cunningham, I. Hunter, P. Tosch, E. Linfield, and A. Davies, "On-chip pulsed terahertz systems and their applications," *International Journal of Infrared and Millimeter Waves*, Vol. 27, No. 4, 557–569, 2006.
7. Neshat, M., D. Saeedkia, R. Sabry, and S. Safavi-Naeini, "An integrated continuous-wave terahertz biosensor," *Proceedings of SPIE*, Vol. 6549, 65490E, 2007.
8. Lu, J., L. Chen, T. Kao, H. Chang, H. Chen, A. Liu, Y. Chen, R. Wu, W. Liu, J. Chyi, et al., "Terahertz microchip for illicit drug detection," *IEEE Photonics Technology Letters*, Vol. 18, No. 21/24, 2254, 2006.
9. Nagel, M., P. Bolivar, M. Brucherseifer, H. Kurz, A. Bosserhoff, and R. Büttner, "Integrated THz technology for labelfree genetic diagnostics," *Applied Physics Letters*, Vol. 80, 154, 2002.
10. Oppenheim, A. V. and R. W. Schafer, *Discrete-time Signal Processing*, Prentice Hall, 1999.
11. Haykin, S., *Blind Deconvolution*, Prentice Hall, 1994.
12. Bell, A. and T. Sejnowski, "An information-maximization approach to blind separation and blind deconvolution," *Neural Computation*, Vol. 7, No. 6, 1129–1159, 1995.

13. Ayers, G. and J. Dainty, "Interative blind deconvolution method and its applications," *Optics Letters*, Vol. 13, No. 7, 547, 1988.
14. Vaseghi, S., *Advanced Signal Processing and Digital Noise Reduction*, Wiley Chichester, 1996.
15. Fletcher, J. R., G. P. Swift, D. C. Dai, J. M. Chamberlain, and P. C. Upadhya, "Pulsed terahertz signal reconstruction," *Journal of Applied Physics*, 113105-1-8, Dec. 2007.
16. Hirsch, O., P. Alexander, and L. Gladden, "Techniques for cancellation of interfering multiple reflections in terahertz time-domain measurements," *Microelectronics Journal*, Vol. 39, No. 5, 841–848, 2008.
17. Heidari, A., "Systems and methods for blind echo cancellation," US Patent No. 12/575,184, 2009.
18. Dorney, T., R. Baraniuk, and D. Mittleman, "Material parameter estimation with terahertz time-domain spectroscopy," *Journal of the Optical Society of America A*, Vol. 18, No. 7, 1562–1571, 2001.
19. Scheller, M., C. Jansen, and M. Koch, "Analyzing sub-100-μm samples with transmission terahertz time domain spectroscopy," *Optics Communications*, Vol. 282, No. 7, 1304–1306, 2009.
20. Saleh, B. E. A. and M. C. Teich, *Fundamentals of Photonics*, John Wiley & Sons, 2007.
21. Agilent Technologies, http://www.agilent.com.